1D-MnO$_2$, 2D-MnO$_2$ and 3D-MnO$_2$ for low-temperature oxidation of ethanol

Bingyang Bai, Junhua Li*, Jiming Hao

State Key Joint Laboratory of Environment Simulation and Pollution Control, School of Environment, Tsinghua University, Beijing 100084, China

ARTICLE INFO

ABSTRACT

1D-MnO$_2$ synthesized using the hydrothermal method was a single-crystal nano-rod with a tetragonal structure. 2D-MnO$_2$ and 3D-MnO$_2$ prepared by the hard template method possess 2D and 3D pore channels, respectively, good pore size distributions and orderly polycrystalline walls due to perfect replication of their templates containing hexagonal (p6mm) pore channel structures and symmetrical cubic (ia3d) structures, respectively. The physicochemical properties of these samples were characterized, and their low-temperature activities for ethanol oxidation were evaluated. 3D-MnO$_2$ exhibited the best catalytic properties for ethanol oxidation due to better low-temperature reducibility and more abundant surface-adsorbed oxygen species and Mn^{4+} ions. The complete oxidation of ethanol to CO$_2$ was achieved at 150 °C on 3D-MnO$_2$. The turnover frequency (TOF) of 3D-MnO$_2$ was the highest (i.e., 0.019 h^{-1} at 40 °C, 0.047 h^{-1} at 70 °C and 0.17 h^{-1} at 110 °C), and its apparent activation energy for the reaction was the lowest (i.e., 28.2 kJ/mol). After the addition of 10 vol.% H$_2$O, the complete oxidation of ethanol to CO$_2$ was obtained at 190 °C on 3D-MnO$_2$. There was no obvious decrease after the sample was run for 160 h. The mesoporous MnO$_2$ catalysts, especially 3D-MnO$_2$, are very promising materials for the efficient elimination of ethanol.

© 2014 Elsevier B.V. All rights reserved.

1. Introduction

Volatile organic compounds (VOCs) emitted from the chemical and textile industries, paints and printing, coatings and motor vehicles are considered to be substantial contributors to air pollution and photochemical pollution [1–4]. Ethanol is a widely used solvent and exists in exhaust gases from ethanol-fueled vehicles [4,5]. Catalytic oxidation is one of the most promising technologies for the elimination of ethanol and other VOCs, which can be oxidized into carbon dioxide and water at much lower temperatures, and no secondary pollution products are generated [6]. The key issue is the choice of catalysts. Recently, the catalytic materials used in ethanol catalytic oxidation are primarily metal oxides and noble metals, such as Pt/Al$_2$O$_3$ [1], OMS-2 [4], CuO/Fe$_2$O$_3$ [5], CuO/MnO$_x$ [7], LaCoO$_3$ [8], Ce$_{1-x}$Mn$_x$O$_2$ [9], LaCo$_{1-y}$Fe$_y$O$_{3\pm\lambda}$ [10], MnCu/ZrO$_2$ [11], M/TiO$_2$ (M = Pt, Pd, Ir, Rh and Au) [12], LaMnO$_3$ [13], Mn$_{0.6}$Ce$_{0.4}$O$_2$ [14], Rh/Al$_2$O$_3$ [15], Ag/La$_{0.6}$Sr$_{0.4}$MnO$_3$ [16], La$_{0.8}$Sr$_{0.2}$MnO$_{3+x}$ [17], CuMn$_2$O$_4$/Al$_2$O$_3$ [18], CuO/Al$_2$O$_3$ [19], MnO$_x$ [20], MnO$_x$–CeO$_2$ [21] and MnCuO$_x$ [22], etc.

Catalytic materials with different morphologies or structures possess special properties. Compositionally identical materials with differing morphologies, such as tubes, sheets, flowers, rods, spheres and pores, have been reported in the literature [23–28]. In the past decade, more and more attention has been focused on mesoporous metal oxides due to their special skeletal structure and large surface area as well as their controllable pore diameter and volume. The materials are templated by mesoporous silica. They are only limited to transition metal oxides, such as NiO, Co$_3$O$_4$, Fe$_2$O$_3$, MnO$_2$, Fe$_3$O$_4$ and Cr$_2$O$_3$ [29–34]. These limitations exist because the target metal oxides are either unreactive with HF or the NaOH solutions or because the precursor material cannot combine with silica. For example, the preparation of mesoporous lithium oxide was impossible [33,35].

Transition metal oxides catalysts, such as MnO$_2$, exhibit good catalytic activity and are cheaper than noble metal catalysts with a high sintering resistance [36,37,20,38,39]. In nature, MnO$_2$ exhibits nonporous morphologies, such as the α, β, γ and δ types. However, synthetic shapes, such as tubes, wires, rods spheres and pores, exhibit enhanced performance in catalysis and applications for photoelectric devices [6,40–42]. The catalytic oxidation of ethanol on mesoporous MnO$_2$ catalysts with different structures has not yet been reported in the literature. Mesoporous MnO$_2$ is applied to the oxidation of ethanol due to its special structure and large surface

area, which may make it more advantageous than nonporous metal oxides or noble metal catalysts. In this work, two-dimensional (2D) and three-dimensional (3D) ordered mesoporous MnO_2, which had well-proportioned pore systems, good pore size distributions and disorderly polycrystalline walls, were prepared using a nanocasting method. In addition, 1D-MnO_2, which possessed a single-crystalline nanostructure, was also synthesized using the hydrothermal method. The catalysts were analyzed by XRD, N_2 adsorption–desorption, SEM and TEM. Their low-temperature catalytic activities for ethanol oxidation were evaluated.

2. Experimental

2.1. Material preparation

Synthesis of SBA-15 and KIT-6 mesoporous silica [43,44]. Typical syntheses methods of the materials were concretely described elsewhere (see Supporting Information).

Nanocasting preparation of mesoporous 2D-MnO_2 and 3D-MnO_2 [23]. In a typical synthesis, 4.0 g of the SBA-15 or KIT-6 molecular sieve were added to a $Mn(NO_3)_2 \cdot 4H_2O$ ethanol solution (0.91 mol/L, 40 mL). The samples were evaporated to dryness at 80 °C. The products were calcined at 200 °C for 6 h. These casting and evaporating steps were repeated. Finally, the materials were calcined at 400 °C for 6 h. The SBA-15 or KIT-6 hard templates were removed using a 2 mol/L NaOH solution. Centrifugal separation was used to eliminate sodium silicate, and the samples were dried at 100 °C and calcined at 400 °C to yield the 2D-MnO_2 and 3D-MnO_2 samples.

Preparation of 1D-MnO_2 [26]. For a typical synthesis, $MnSO_4 \cdot H_2O$ (0.008 mol) and an equal amount of ammonium persulfate ($(NH_4)_2S_2O_8$) were added to distilled water at room temperature to form a homogeneous solution, which was then transferred into a 40 mL Teflon-lined stainless steel autoclave, sealed and maintained at 140 °C for 12 h. After the reaction was completed, the resulting solid product was filtered, washed with distilled water to remove ions that may be in the final products, and finally dried at 120 °C to yield the 1D-MnO_2 sample.

2.2. Material characterizations

XRD patterns were tested on a TTR3 type X-ray diffractometer utilizing a Cu Kα radiation source with a 0.05°/min scanning speed, 40 kV tube voltage and 40 mA tube current. The 2θ of the low-angle and wide-angle XRD ranged from 0.6 to 5° and from 20 to 80°, respectively. The structural parameters, pore size distributions and N_2 adsorption isotherms of the catalysts were measured on an Autosorb-1MP instrument. The samples were pretreated at 300 °C for 4 h under vacuum. The N_2 adsorption–desorption isotherms were obtained using the Barrett-Joyner-Halenda (BJH) method. The SEM images were recorded on a Hitachi S-5500 apparatus at a voltage of 5.0 and 30 kV. The samples were dispersed by ultrasonic waves in distilled water for 10 min and prepared on a lacey carbon film supported by a copper grid. Finally, the samples were calcined at 110 °C for 20 min. The TEM image was recorded on a JEM-2011 instrument at a voltage of 200 kV. The samples were prepared by ultrasonic dispersion in ethanol for 8 min, and the transparent suspended droplets were placed on a copper grid using a capillary. The H_2-TPR was measured on a Chemisorb 2720 apparatus. 0.05 g of the sample (40–60 mesh) was pretreated in N_2 flow at 300 °C for 1 h in a quartz reactor. After the pretreatment, the samples were cooled and reduced in a flow (50 mL/min) of 5% H_2–95% Ar using a temperature range of 30–900 °C with a heating rate of 10 °C/min. The H_2 consumptions of the reduction band were calibrated by a standard CuO (99.998%) powder. The XPS patterns were measured
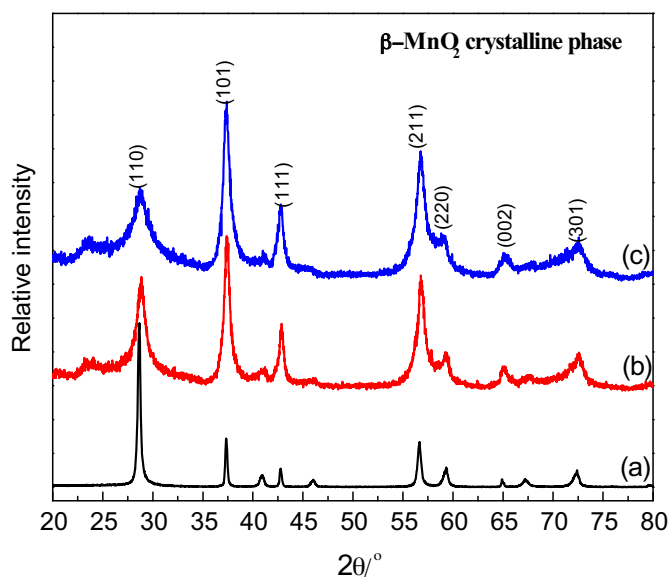

Fig. 1. The wide-angle XRD patterns of (a) 1D-MnO_2, (b) 2D-MnO_2 and (c) 3D-MnO_2.

on a PHI-5300 apparatus at 300 W using Mg Ka X-rays as the excitation source. The C 1s signal at a binding energy (BE) of 284.6 eV was employed as a reference for BE calibration. The ratio of elements with different valence states was calculated based on the peak areas processed by the XPS-PEAK software.

2.3. Evaluation of catalytic activity

The catalytic oxidation activity for ethanol or acetaldehyde was tested in a fixed bed quartz tube reactor (Φ 10 mm) with 0.2 g of catalyst (40–60 mesh). The total flow rate through the reactor was maintained at 150 mL/min using mass-flow meters and included 300 ppm ethanol or 300 ppm acetaldehyde as well as 20% (vol) O_2 and N_2 equilibrium gas. The space velocity of the catalytic oxidation was 45,000 mL/(g h). The products of the reaction were analyzed online by an Agilent 7890A gas chromatograph with a TCD detector consisting of a Porapak-Q column and an FID detector with an HP-INNOWAX column. CO_2 is only analyzed by the TCD detector, and ethanol and acetaldehyde are detected by the FID detector due to its lower limit of detection for organic matter. The conversion was calculated from the proportion of export and import concentrations of ethanol or acetaldehyde. The remaining small amount of products was neglected except for acetaldehyde and CO_2. For kinetic measurements, the ethanol conversion was maintained below 15% under the addition of 500 ppm ethanol, 20 vol.% O_2, N_2 as the balance gas, and GHSV = 120,000 mL/(g h). The TOF was defined as the number of ethanol molecules converted per Mn^{4+} ions per hour.

$$\text{TOF} = \frac{C_{\text{ethanol}} X_{\text{ethanol}} V_{\text{gas}}}{n_{\text{Mn}^{4+}}} [\text{h}^{-1}] \qquad (1)$$

where C_{ethanol}: concentration of ethanol in gas mixture; X_{ethanol}: ethanol conversion; V_{gas}: total molar flow rate; $n_{\text{Mn}^{4+}}$: mole number of Mn^{4+} ions calculated by H_2-TPR.

3. Results and discussion

3.1. Textural characterization of the catalysts

The wide-angle XRD patterns of 1D-MnO_2, 2D-MnO_2 and 3D-MnO_2 are shown in Fig. 1. All of the materials exhibit diffraction peaks at 28.7°, 37.3°, 42.8°, 56.7°, 59.4°, 64.8° and 72.3° (2θ), which correspond to the (1 1 0), (1 0 1), (1 1 1), (2 1 1), (2 2 0), (0 0 2) and

Table 1
Physical parameters of mesoporous silica and different MnO_2 catalysts.

Sample	Crystal sizes[a] d_{211} (nm)	Lattice parameters[b] a (nm)	Surface areas[c] A_{BET} (m²/g)	Pore volumes V_p (cm³/g)	Pore diameters[d] D_P (nm)	Wall thickness[e] D_W (nm)
SBA-15	–	9.90	579	1.23	7.5	2.4
KIT-6	–	21.63	695	0.64	3.7/5.9	3.5
1D-MnO₂	26.5	–	21	–	–	–
2D-MnO₂	11.6	10.14	45	0.20	3.7	4.0
3D-MnO₂	9.5	20.85	87	0.27	3.7/11.4	8.2

[a] Crystal sizes of 1D-MnO₂, 2D-MnO₂ and 3D-MnO₂ calculated through Scherrer formulation from half peak width of the (2 1 1) diffraction peak in the XRD patterns.
[b] Lattice parameters of 2D-MnO₂ and 3D-MnO₂ calculated from the d_{100} and d_{211} spacing in the XRD patterns, respectively.
[c] Surface areas calculated by the BET method.
[d] Pore sizes obtained from the N₂ adsorption isotherms by the BJH method.
[e] Wall thickness of SBA-15, KIT-6, 2D-MnO₂ and 3D-MnO₂ obtained by subtraction of the pore size from the lattice parameter, reference [30] and TEM images, respectively.

(3 0 1) planes, respectively. The diffraction peaks indicate that the materials consist of a β-MnO_2 crystalline phase, which corresponds to pyrolusite with a rutile structure [32,42]. From Table 1, the average crystal sizes of the samples were calculated using the Scherrer formulation from the half peak width of the (2 1 1) diffraction peak. The crystal size of 3D-MnO₂ is the lowest (9.5 nm), and the crystal size of 1D-MnO₂ is the highest (26.5 nm). The smaller crystal size of 3D-MnO₂ will likely enhance the catalytic ability for ethanol oxidation.

Fig. 2 shows the low-angle XRD patterns for 2D-MnO₂ and 3D-MnO₂. The 100 and 220 diffraction peaks of 2D-MnO₂ and 3D-MnO₂ correspond to 1.00° and 1.04° (2θ), respectively. 2D-MnO₂ exhibits a characteristic 2D hexagonal (p6mm) mesoporous structure. The unit cell parameter of 2D-MnO₂, which is calculated from the 100 diffraction, is 10.14 nm. This value is nearly equal to the unit cell parameter of the SBA-15 template (a = 9.90 nm), which confirms that 2D-MnO₂ is a replica of the SBA-15 mesoporous silica (Fig. S1). 3D-MnO₂ Exhibits 211 and 332 diffraction peaks, which are characteristic of 3D ordered mesoporous structures with cubic symmetry (ia3d). The unit cell parameter of 3D-MnO₂, which was calculated from the 211 diffraction, is 20.85 nm, and the unit cell parameter of KIT-6 is 21.63 nm. The two numbers are nearly equal, which confirms that 3D-MnO₂ successfully replicates the 3D mesoporous structure of the KIT-6 silica (Fig. S2). In addition, the corresponding 100 and 211 diffraction intensities measured in 2D-MnO₂ and 3D-MnO₂ are weaker than those of their templates, which indicates that their structural orders are different from SBA-15 and KIT-6.

Fig. 3 shows the N₂ adsorption/desorption isotherms and pore size distributions for 2D-MnO₂ and 3D-MnO₂. All of the N₂ adsorption/desorption isotherms from the materials have hysteresis rings

and are type IV [29–34]. These properties indicate that they are mesoporous materials, which is consistent with the low-angle XRD results. The isotherms for 2D-MnO₂ and 3D-MnO₂ are different from their corresponding templates (Figs. S3 and S4), which is most likely due to interparticle voids [31]. The inset in Fig. 3 shows the BJH pore size distribution, which is calculated from the desorption isotherms. The 2D-MnO₂ shows 3.7 nm of pore size at a maximum distribution and 4.0 nm of wall thickness, and the SBA-15 template shows 7.5 nm of pore size and 2.4 nm of wall thickness (Table 1). The pore size of 3D-MnO₂ is 3.7 nm and 11.4 nm at a maximum distribution, and the analogous values for the KIT-6 template are 3.7 and 5.9 nm, respectively (Table 1). The wall thickness of 3D-MnO₂ is 8.2 nm from the TEM images. The pore characteristics of 2D-MnO₂ and 3D-MnO₂ result from a replication of their corresponding SBA-15 and KIT-15 templates. The pore sizes of the 2D-MnO₂ and 3D-MnO₂ correspond with the thickness of the framework of their templates, and the wall thickness of the 2D-MnO₂ and 3D-MnO₂ correspond with the pore size of their templates. After nanocasting a sample, the manganese material in the pore systems is collected in the same sample regions to form a metal oxide phase, which coexists with the silica skeleton. After template removal, the crystallite regions composed of bulk silica become the pore channels and the regions composed of MnO_2 become the crystalline walls. The pore size of 3D-MnO₂ is larger than the wall thickness of KIT-6 (Table 1), probably due to the double pore system of 3D-MnO₂ to cause crystal phase rearrangement. Table 1 lists the physical parameters of the mesoporous silica and all three samples. 1D-MnO₂ has the
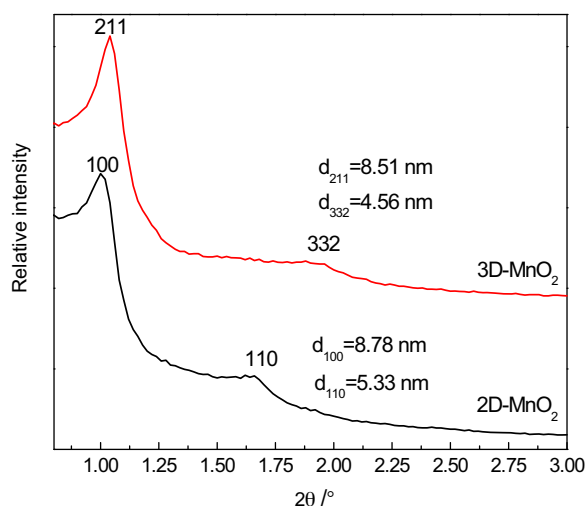

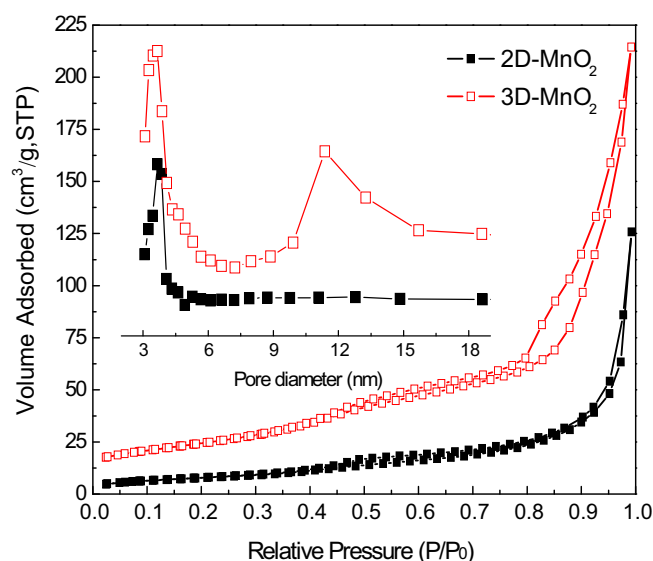**Fig. 2.** The low-angle XRD patterns of 2D-MnO₂, and 3D-MnO₂.

Fig. 3. N₂ adsorption/desorption isotherms and pore size distributions of 2D-MnO₂ and 3D-MnO₂.

smallest surface area of $21 \, m^2/g$. 2D-MnO$_2$ and 3D-MnO$_2$ have smaller BET surface areas and pore volumes than the mesoporous silica, and their BET surface areas are 45 and $87 \, m^2/g$, respectively. The reason for this disparity is due to the density of bulk MnO$_2$ being higher than in bulk silicon and the mesoporous MnO$_2$ losing a portion of the structure when the hard template was removed. The missing structure is composed of incompletely eliminated silica, which is demonstrated by the following SEM images.

The surface structure of mesoporous silica, 1D-MnO$_2$, 2D-MnO$_2$ and 3D-MnO$_2$ are shown in Fig. 4. 1D-MnO$_2$ is a nonporous material and has a one-dimensional single-crystal nanostructure with diameters of 40–100 nm and lengths ranging between 0.2 and 1.5 μm (Figs. 4a and b). The formation of the 1D character results from the hydrothermal method through the oxidation of Mn^{2+} by S$_2$O$_8^{2-}$ under the addition of selected-control low-temperature and no existence of templates [26]. 2D-MnO$_2$ (Figs. 4c–e) is a 2D ordered mesoporous material, and its morphology and pore structure are the same as that of the SBA-15 template (Figure S5a in the Supporting Information). The 2D character of 2D-MnO$_2$ is attributed to a complete replica of the SBA-15 template with a 2D hexagonal channel structure. The SEM images of 3D-MnO$_2$ are shown in Fig. 4f–h. Based on these images, 3D-MnO$_2$ clearly possesses a 3D ordered pore channel structure. The formation of 3D character in 3D-MnO$_2$ is due to a perfect replication of the KIT-6 template, which has a symmetrical 3D structure with double pore systems. From the SEM image of KIT-6 (Fig. S5b in the Supporting Information), each hole connects to two unlimited pore crossroad-like channels, which are connected to each other through smaller holes [30]. The pore size of 3D-MnO$_2$ at two maximum distributions is shown in the inset of Fig. 3. The unrestricted access to the 2D and 3D pore system from the surface is clearly illustrated in the SEM images.

The TEM image (Fig. 5a) for 1D-MnO$_2$ exhibits nano-rods of a single crystal with a tetragonal structure, which are viewed along the [001] direction. 1D-MnO$_2$ has (1 1 0) crystal planes with a lattice spacing of 0.311 nm (Fig. 5b). For mesoporous MnO$_2$, the SEM images provide a 3D view of the pore structure, while the TEM images reveal the 2D properties of the material. The TEM images (Figs. 5c, e) for 2D-MnO$_2$, which are viewed along the [111] direction, confirm that the 2D ordered hexagonal structure exists over a large area. When viewed down the [110] direction, the image in Fig. 5d reveals highly ordered hexagonal arrays of mesopores with one-dimensional channels. The top right corner in Fig. 5c shows the fast Fourier transform (FFT) of 2D-MnO$_2$ and confirms that it is a perfect replica of SBA-15. The cell diameter estimated from the TEM images is approximately 10.12 nm, which agrees with the value calculated from the d_{100} spacing in the XRD pattern (Table 1). The FFT inset in Fig. 5d exhibits diffraction rings composed of non-continuous points, which reveals that 2D-MnO$_2$ possesses a disordered polycrystalline wall. The (1 1 0) crystal planes and the (1 0 1) crystal plane with a lattice spacing of 0.240 nm (inset, Fig. 5e) are exposed in 2D-MnO$_2$. Figs. 5f, h and g are views along the [111] and [100] directions, respectively. Along with the results of FFT diffraction (inset, Fig. 5f), this image confirms the existence of an ordered cubic (ia3d) mesoporous structure. The lattice dimension (19.66 nm), which was observed by TEM, matches the value calculated from the d_{211} spacing in the XRD pattern (Table 1). The electron diffraction pattern in Fig. 5g demonstrates that 3D-MnO$_2$ also has a disordered polycrystalline wall. In addition, 3D-MnO$_2$ also exposes the (1 1 0) and (1 0 1) crystal planes (inset, Fig. 5h). In the unit cell of β-MnO$_2$, the (1 1 0) crystal facets expose more Mn^{4+} ions than the other planes [45,46]. The various structures of the samples may result in various Mn^{4+} contents on the exposed (1 1 0) crystal facets. We infer that 3D-MnO$_2$ has more surface Mn^{4+} ions, which most likely provides sufficient active sites for the ethanol oxidation reaction.

3.2. X-ray photoelectron spectroscopy and thermal reduction of the catalysts

Fig. 6 is the Mn and O X-ray photoelectron spectroscopy diagram of the various MnO$_2$ catalysts. Fig. 6A shows that Mn 2p$_{2/3}$ has two components displayed in BE at 641.6 and 642.9 eV, which are due to the surface Mn^{3+} and Mn^{4+} ions, respectively [14]. From Table 2, the surface Mn^{4+}/Mn^{3+} molar ratios of 1D-MnO$_2$, 2D-MnO$_2$ and 3D-MnO$_2$ are 1.31, 1.63 and 3.85, respectively. The 3D-MnO$_2$ catalyst has the highest surface Mn^{4+}/Mn^{3+} molar ratios, and the 1D-MnO$_2$ displays has the lowest ratios. This result indicates that the surface of mesoporous MnO$_2$, especially 3D-MnO$_2$, exposes more abundant surface Mn^{4+} species. More surface Mn^{4+} ions may increase the oxygen vacancies of an oxide material, which is beneficial to the adsorption, activation and migration of oxygen in the gas phase. The O1s signals displayed in BE were observed at 529.3 and 531.3 eV, as shown in Fig. 6B. The former value corresponds to surface lattice oxygen (O$_{latt}$), and the latter value corresponds to surface adsorbed oxygen (O$_{ads}$) [6]. As reported in Table 2, the surface O$_{ads}$/O$_{latt}$ molar ratios of 1D-MnO$_2$, 2D-MnO$_2$ and 3D-MnO$_2$ are 0.31, 0.61 and 0.97, respectively. Therefore, the surface of 3D-MnO$_2$ has the most abundant surface adsorbed oxygen species followed by 2D-MnO$_2$. Surface active oxygen species play an important role in oxidation reactions [47,48]. Mesoporous MnO$_2$, especially 3D-MnO$_2$, has many more surface adsorbed oxygen species. The formation of oxygen adsorbed species most likely results from the presence of surface oxygen vacancies on the different MnO$_2$ catalysts. These oxygen vacancies are related to the coexistence of Mn^{3+} and Mn^{4+} ions. The surface oxygen vacancy density may be the highest on 3D-MnO$_2$ due to it possessing the most surface adsorbed oxygen species. Abundant surface adsorbed oxygen species are easily stripped at low temperature and are favorable for stronger reducibility to enhance the oxidation performance. XPS can only quantify elements on the surface of a material. The pore structure and larger specific surface area of the mesoporous MnO$_2$ catalysts do not have an edge. However, if the channel structure and specific surface area in the bulk phase of mesoporous MnO$_2$ is considered, 3D-MnO$_2$ should possess many more surface adsorbed oxygen species.

The H$_2$-TPR patterns of the different MnO$_2$ catalysts are shown in Fig. 7A. The reduction peaks of 1D-MnO$_2$ were located at 380 °C and 447 °C and correspond to H$_2$ consumptions of 7.24 and 4.12 mmol/g, respectively (Table 2). The reduction peaks of 2D-MnO$_2$ were located at 343 and 439 °C and correspond to H$_2$ consumptions of 6.35 and 3.74 mmol/g, respectively (Table 2). 1D-MnO$_2$ and 2D-MnO$_2$ exhibit two reduction peaks due to the reduction of MnO$_2$ to Mn$_2$O$_3$ (peak 1) and Mn$_2$O$_3$ to MnO (peak 2). 3D-MnO$_2$ exhibits three reduction peaks located at 310 °C, 350 °C and 432 °C due to the reduction of MnO$_2$ to Mn$_2$O$_3$ (peak 1), Mn$_2$O$_3$ to Mn$_3$O$_4$ (peak 2) and Mn$_3$O$_4$ to MnO (peak 3), and correspond to H$_2$ consumptions of 3.24, 3.43 and 3.66 mmol/g, respectively (Table 2). In this study, the total H$_2$ consumption of the samples is quite close to their theoretical H$_2$ consumption (11.5 mmol/g), indicating that a substantial fraction of Mn^{4+} ions in the catalysts have been reduced. H$_2$ consumption for peak 1 from Mn^{4+} to Mn^{3+} can indicate the number of Mn^{4+} ions. The H$_2$ consumptions for peak 1 of 1D-MnO$_2$ (7.24 mmol/g) are larger than that of 2D-MnO$_2$ (6.35 mmol/g). For this reason, mesoporous MnO$_2$ contain Si impurity and have a smaller reduced mass. If no silica exists in the mesoporous MnO$_2$ and all of the samples with the same mass pure MnO$_2$ in the H$_2$—TPR test, 2D-MnO$_2$ should have higher H$_2$ consumptions and more Mn^{4+} ions than 1D-MnO$_2$. In comparison to 2D-MnO$_2$, 3D-MnO$_2$ exhibits peak 2 at 350 °C due to a special disproportionation reaction of Mn$_2$O$_3$ (III) to Mn$_3$O$_4$ (IV and II). The dismutation is related to more abundant surface oxygen adspecies. If the dismutation is taken into consideration, the sum
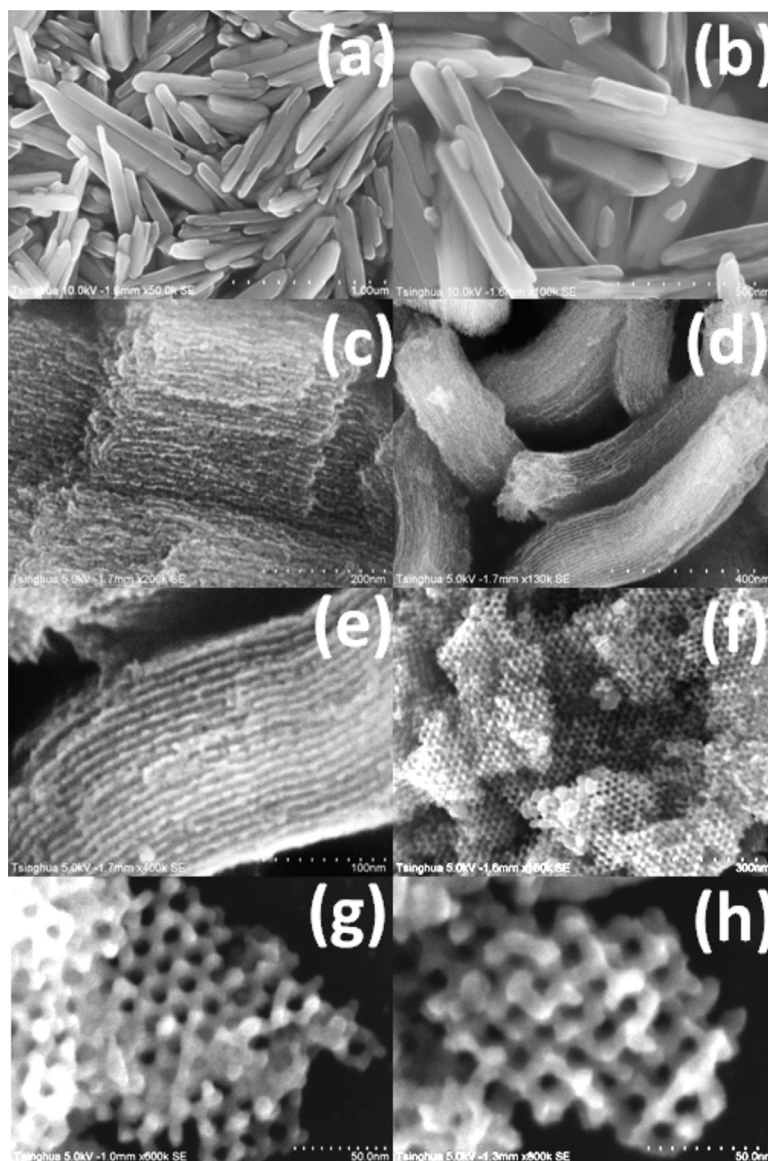
Fig. 4. SEM images of 1D-MnO$_2$ (a, b), 2D-MnO$_2$ (c–e) and 3D-MnO$_2$ (f–h).

(6.9 mmol/g) of H$_2$ consumptions of peak 1 and peak 3 (Mn$_3$O$_4$ to MnO) will confirm that the quantity of Mn^{4+} ions in the 3D-MnO$_2$ is higher than that in the 2D-MnO$_2$. In addition, H$_2$ consumption of peak 2 is for 3D-MnO$_2$ lower than for 2D-MnO$_2$ and 1D-MnO$_2$ (Table 2), indicating that 3D-MnO$_2$ possesses less Mn^{3+} ions. Less Mn^{3+} ions imply more Mn^{4+} ions. Combined with the XPS analyses, it is concluded that Mn^{4+} ions in 3D-MnO$_2$ have slightly more than that in 2D-MnO$_2$. From Table 2, the reduction temperature of 3D-MnO$_2$ is the lowest followed by 2D-MnO$_2$. This result indicates that 3D-MnO$_2$ possesses excellent low-temperature reducibility. The results in Fig. 7B indicate that 3D-MnO$_2$ exhibits a much higher initial H$_2$ consumption rate, which further confirms that the 3D-MnO$_2$ has the stronger reducibility, and oxygen adsorbed species connected to Mn^{4+} ions are more easily desorbed and can combine with hydrogen. Therefore, the 3D-MnO$_2$ catalyst may exhibit excellent catalytic performance for ethanol oxidation.

Table 2
Reduction temperatures, H$_2$ consumptions and surface element composition of different MnO$_2$ catalysts.

Sample	Reduction temperature (°C)[a]			H$_2$ comsumption (mmol/g)[b]				Mn^{4+} active site number[c] (mmol)	Surface element molar ratio[d]	
	Peak 1	Peak 2	Peak 3	Peak 1	Peak 2	Peak 3	Total		Mn^{4+}/Mn^{3+}	O$_{ads}$/O$_{latt}$
1D-MnO$_2$	380	447	–	7.24	4.12	–	11.36	1.5	1.31	0.31
2D-MnO$_2$	343	439	–	6.35	3.74	–	10.09	1.3	1.65	0.61
3D-MnO$_2$	310	350	432	3.24	3.43	3.66	10.33	1.4	3.85	0.97

[a] Reduction temperatures corresponding to the maximum values of reduction peaks in the H$_2$-TPR result.
[b] H$_2$ consumptions calculated by reduction peak areas.
[c] Mn^{4+} ions were calculated by the H$_2$-TPR result.
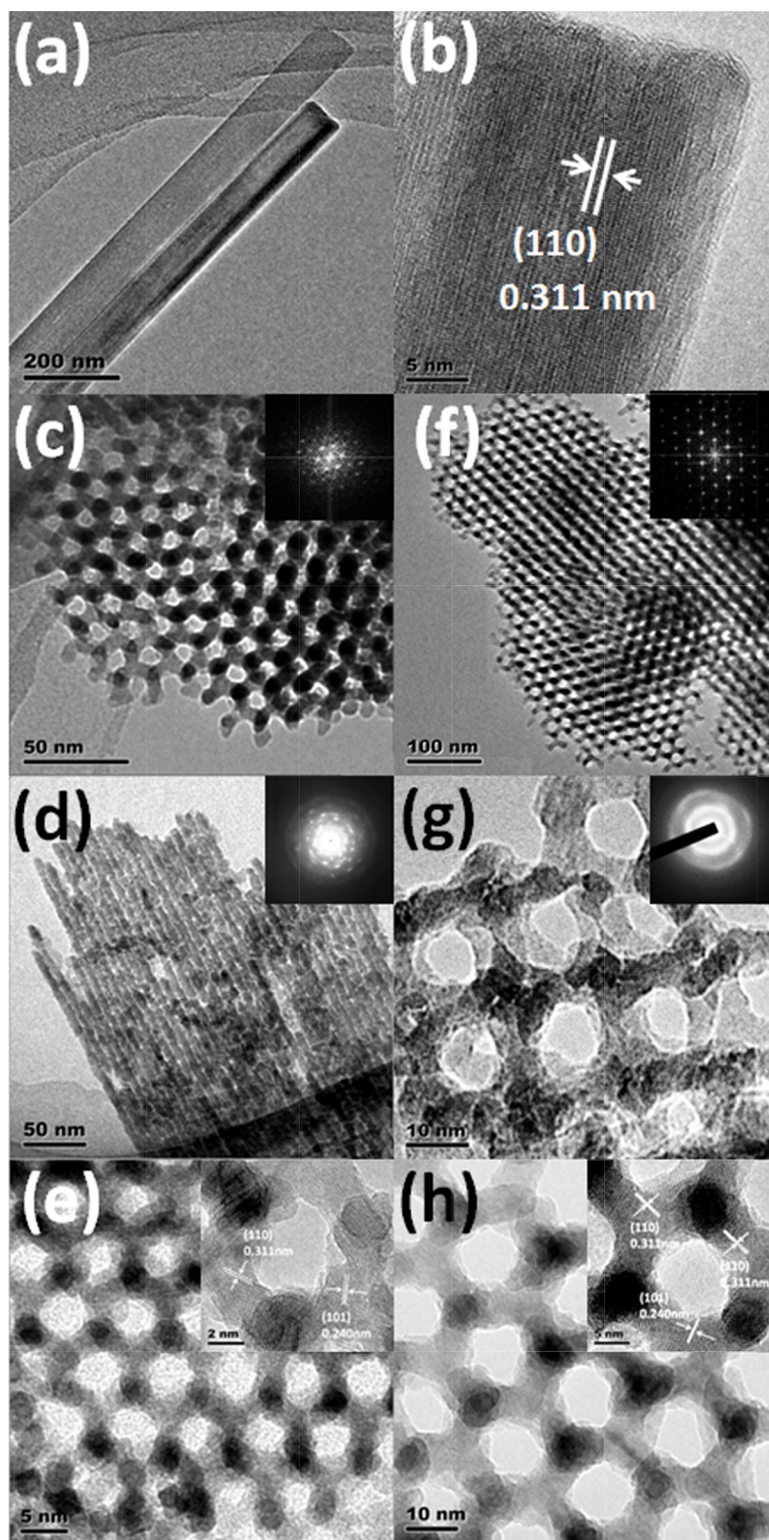[d] Surface element molar ratio calculated by peak areas of XPS.

Fig. 5. TEM images of 1D-MnO$_2$ (a, b), 2D-MnO$_2$ (c–e) and 3D-MnO$_2$ (f–h).

3.3. Oxidation performance of ethanol on the different MnO$_2$ catalysts

The ethanol and acetaldehyde catalytic oxidation activities of the different MnO$_2$ catalysts are shown in Fig. 8. The ethanol conversion at the lowest temperature was 40% on 3D-MnO$_2$, 28% on 2D-MnO$_2$, and 20% on 1D-MnO$_2$, and complete conversion was observed at 140 °C on 3D-MnO$_2$, at 150 °C on 2D-MnO$_2$, and at 170 °C on 1D-MnO$_2$ (Fig. 8A). The complete oxidation of ethanol to CO$_2$ was achieved at 150 °C on 3D-MnO$_2$, at 160 °C on 2D-MnO$_2$, and at 200 °C on 1D-MnO$_2$ (Fig. 8C). From Fig. 8B, the maximum value of the acetaldehyde yield was observed at 100 °C on 3D-MnO$_2$, at 110 °C on 2D-MnO$_2$, and at 140 °C on 1D-MnO$_2$. Acetaldehyde is the major intermediate species in ethanol oxidation.
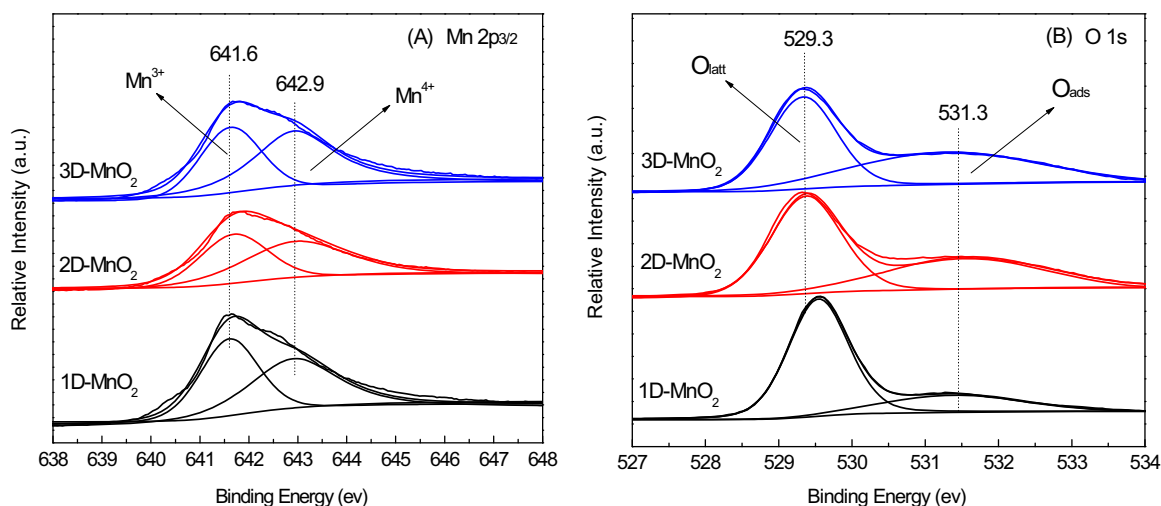
Fig. 6. XPS pattern of 1D-MnO_2, 2D-MnO_2 and 3D-MnO_2.

To further explain the catalytic property of ethanol oxidation, the results from acetaldehyde oxidation are in Fig. 8D. Complete oxidation of acetaldehyde to CO_2 was observed at 150 °C on 3D-MnO_2, at 160 °C on 2D-MnO_2, and at 190 °C on 1D-MnO_2. To further compare the catalytic performance, Fig. 9A shows that the TOF of 3D-MnO_2 is 0.019 h^{-1} at 40 °C, which gradually increases to 0.047 h^{-1} at 70 °C. As the temperature increases, the TOF rapidly soars to 0.17 h^{-1} at 110 °C. The TOF of 2D-MnO_2 is 0.013 h^{-1} at 40 °C, increase to 0.038 h^{-1} at 70 °C, and promptly increases up to 0.14 h^{-1} at 110 °C. The TOF for 1D-MnO_2 is the lowest (i.e., only 0.03 h^{-1} at 110 °C). 3D-MnO_2 has the highest rate per Mn^{4+} ion. For this reason, a larger number of Mn^{4+} ions in the 3D-MnO_2 are one of the main factors influencing catalytic performance. In general, the oxidation reaction first occurs on the surface of the metal oxide. The oxygen in the metal oxide cannot be the active site because it participates in the process. A single β-MnO_2 catalyst consists of a peculiar sharing of [MnO_6] octahedral chains [45]. Mn^{4+} ions are most likely the active sites of ethanol catalytic oxidation because the oxidation reaction often occurs through redox recycles of high and low valence state cations, such as Co^{3+}/Co^{2+} [24], Mn^{4+}/Mn^{3+} [49], and Ce^{4+}/Ce^{3+} [50]. The redox recycling of Mn^{3+}/Mn^{2+} is impossible due to the higher reduction temperature from Mn^{3+} to Mn^{2+} in the H_2-TPR result. Mn^{4+} ions are the high valence state in MnO_2. We believe that in the 3D-MnO_2 catalyst, the Mn^{4+} ions provide

sufficient active sites for the oxidation of ethanol and the redox cycle for Mn^{4+}/Mn^{3+} occurs in the process. Fig. 9B shows the Arrhenius plots for ethanol oxidation on the different MnO_2 catalysts. The apparent activation energy of the reaction is 52.8 kJ/mol on 1D-MnO_2, 33.6 kJ/mol on 2D-MnO_2 and 28.2 kJ/mol on 3D-MnO_2. The apparent activation energy of 3D-MnO_2 is the lowest, which indicates that surface adsorbed oxygen species are easily activated at low temperatures and participate in the oxidation reaction. This result is consistent with the H_2-TPR result. Table S1 lists the ethanol conversion for the kinetics measurement. The mesoporous MnO_2 catalysts, especially 3D-MnO_2, are potentially advantageous due to their special porous structure and larger surface areas, which is highly conducive to ethanol oxidation. The 3D-MnO_2 sample has the best catalytic activity for ethanol followed by 2D-MnO_2.

Fig. 10 shows the effects of the ethanol concentration, space velocity and water vapor on the 3D-MnO_2 catalyst, and the corresponding data are reported in Table S2 in the Supporting Information. From Fig. 10A, when the ethanol concentration is 100 ppm, complete conversion was observed at 120 °C, and complete oxidation of ethanol to CO_2 was observed at 140 °C. These results indicate that the decrease of ethanol concentration can shift the temperature of complete conversion for ethanol oxidation to lower temperature. As shown in Fig. 10B, complete conversion was observed at 120 °C when the space velocity decreased, which
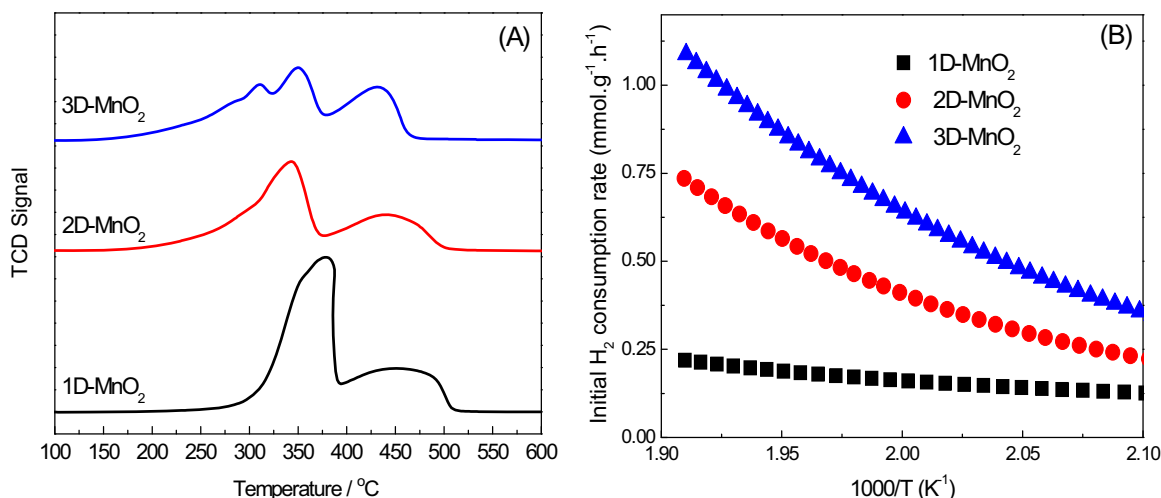

Fig. 7. H_2-TPR pattern (A) and initial H_2 consumption rates (B) of 1D-MnO_2, 2D-MnO_2 and 3D-MnO_2.
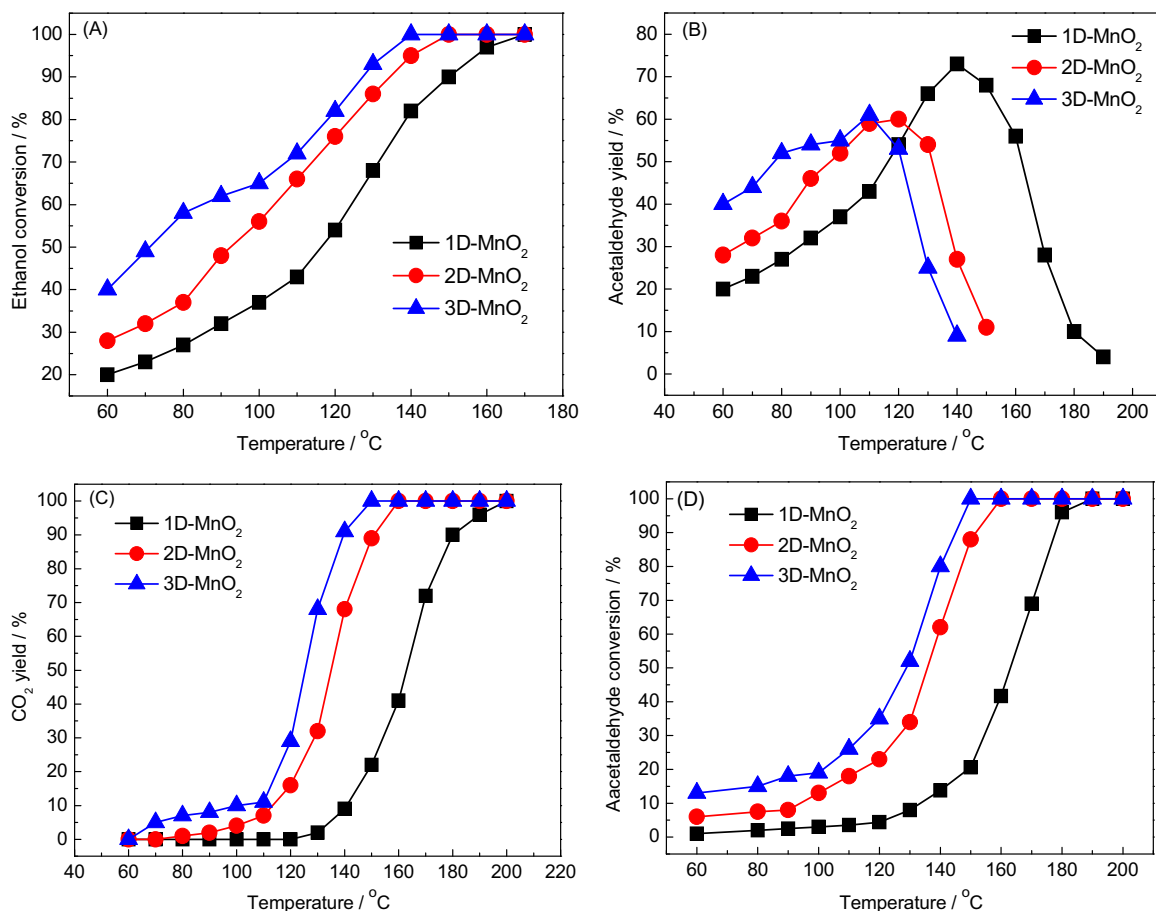
Fig. 8. Ethanol and acetaldehyde catalytic performance of the different MnO_2 catalysts. (A) Ethanol conversion, (B) acetaldehyde yield during ethanol oxidation, (C) CO_2 yield during ethanol oxidation and (D) acetaldehyde conversion during acetaldehyde oxidation; Reaction conditions: 300 ppm ethanol, 300 ppm acetaldehyde, 20 vol.% O_2, N_2 as balance gas, GHSV = 45,000 mL/(g h).

indicated that the activity of the sample increased as the space velocity decreased. Fig. 10C shows the catalytic performance of 3D-MnO_2 after the addition of 10 voc.% H_2O. Complete conversion was observed at 190 °C, and the maximum value of the acetaldehyde yield was achieved at 140 °C. In addition, the complete oxidation of ethanol to CO_2 was observed at 190 °C. The addition of water vapor decreased the catalytic activity, and the complete oxidation

occurred at less than 200 °C. In fact, moisture often exists in exhaust gases from ethanol-fueled vehicles. The funnel of the vehicles can reach 200 °C and higher. A catalyst in automobiles very rapidly warms up at temperatures lower than 200 °C. The temperature reaches 160 °C from a normal temperature within 22 s and 200 °C during the cold start period within 26 s [51]. Therefore, the 3D-MnO_2 catalyst can convert ethanol to CO_2 in the presence of H_2O.
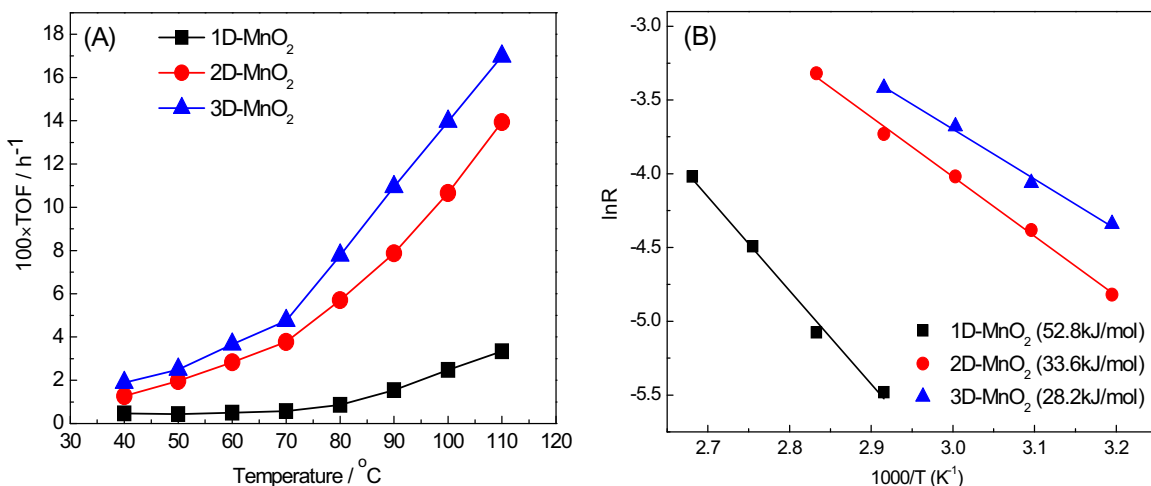

Fig. 9. (A) TOF and (B) Arrhenius plots in ethanol oxidation of 1D-MnO_2, 2D-MnO_2 and 3D-MnO_2. Reaction conditions: 500 ppm ethanol, 20 vol.% O_2, N_2 as balance gas, GHSV = 120,000 mL/(g h).
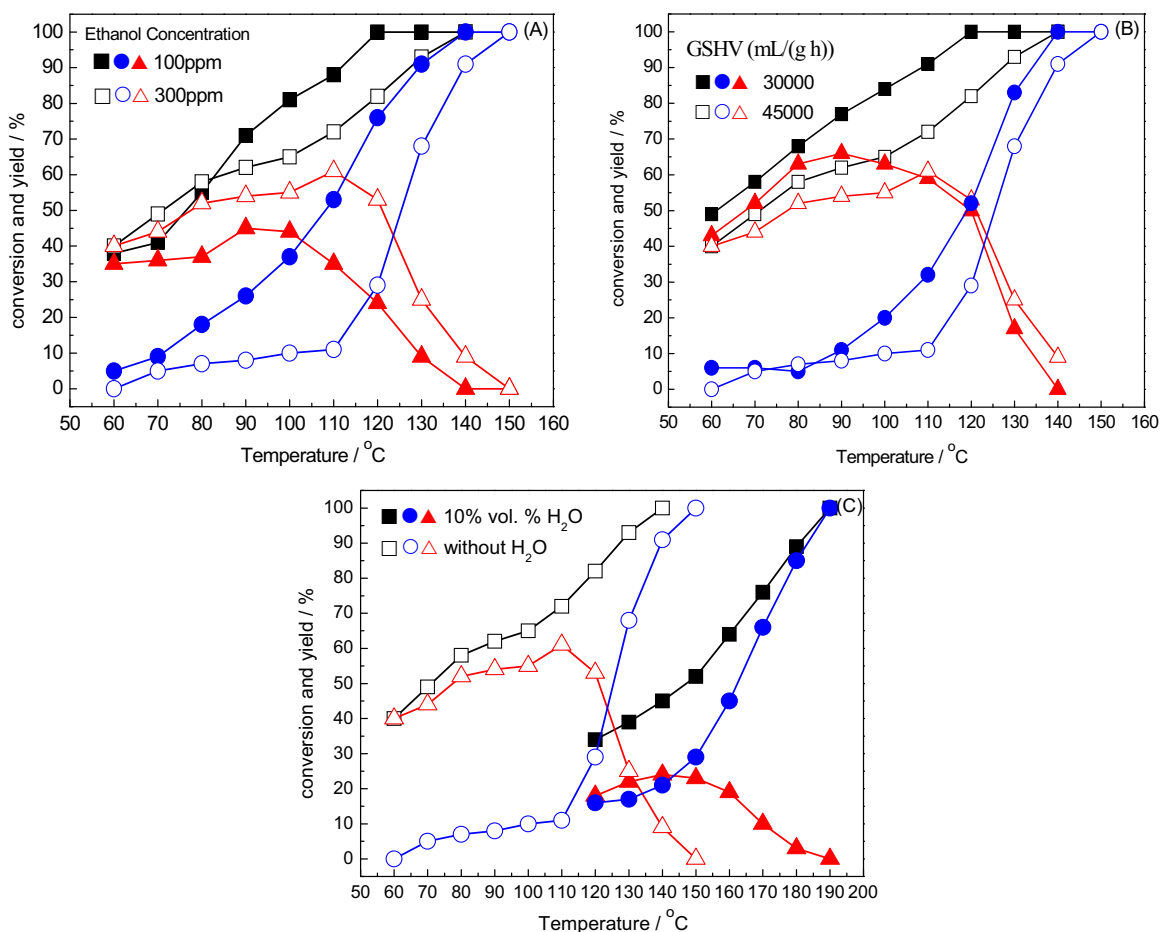
Fig. 10. The effect of performance for (A) ethanol concentration, (B) space velocity and (C) water vapor over the 3D-MnO_2 catalyst under the conditions of 20 vol.% O_2, N_2 as balance gas, (A, C) GHSV = 45,000 mL/(g h), (B, C) 300 ppm ethanol and (C) 10 vol.% H_2O. "■□", "●○" and "▲△" marks stand for ethanol conversion, CO_2 yield and acetaldehyde yield, respectively.

Fig. 11 shows the ethanol catalytic performance as a function of time on stream over the 3D-MnO_2 catalyst. After the addition of 10 vol.% H_2O, there was no significant decrease in the catalytic ability of the sample for 160 h. Therefore, we believe that the 3D-MnO_2 sample was a promising catalytic material for the elimination of ethanol.
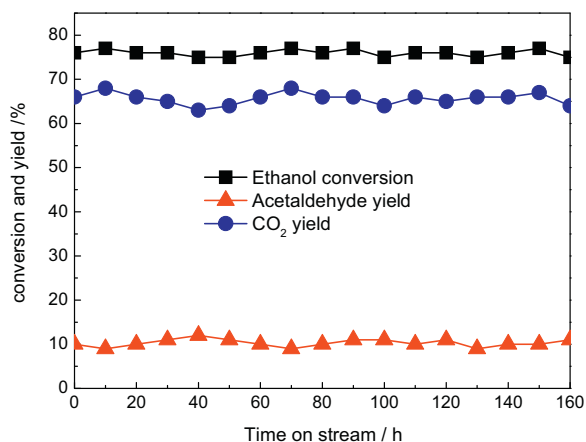

Fig. 11. Ethanol catalytic performance with time on stream over the 3D-MnO_2 catalyst under the conditions of reaction temperature = 170 °C, 10 vol.% H_2O, ethanol concentration = 300 ppm, 20 vol.% O_2, N_2 as balance gas, GHSV = 45,000 mL/(g h).

Special materials with the same compositions and different structures have often been synthesized to change these factors and improve the catalytic ability [24–27]. The catalytic activity for ethanol oxidation on different MnO_2 catalysts decreases in the following order: 3D-MnO_2 > 2D-MnO_2 > 1D-MnO_2, which is consistent with the trend in the crystal size, pore channel, specific surface areas, surface Mn^{4+} ions, surface adsorbed oxygen species and low-temperature reducibility. Although these factors are favorable for the oxidation reaction, only a few determine the catalytic activity of the catalysts. Mesoporous MnO_2 catalysts, especially 3D-MnO_2, have a special pore channel structure, which is beneficial to the adsorption and diffusion of reactants and products. A smaller crystal size and special pore channel can increase the surface area of the catalyst. The BET surface area of 3D-MnO_2 is approximately two times larger than that of 2D-MnO_2 and four times larger than that of 1D-MnO_2, but the normalized activity of 3D-MnO_2 is not much better than that of the 2D-MnO_2 catalyst after deducting surface areas (Table S1). The results indicated that the physical parameters, such as crystal size, pore channel structure and surface area, are minor factors that influence the ethanol catalytic activity. 3D-MnO_2 exhibited better low-temperature reducibility and possessed more Mn^{4+} ions based on the H_2-TPR result. A large number of surface Mn^{4+} ions and adsorbed oxygen species were determined from XPS results. It is well known that low-temperature reducibility is one of the critical factors for the oxidation reaction, and more surface adsorbed oxygen species can improve the catalytic activity [6,52]. For the α-MnO_2 catalyst, either a small amount of Mn^{3+} ions or a large amount of Mn^{4+} ions

are important for high activity in CO oxidation [53], which is similar to ethanol oxidation on 3D-MnO_2. The increase in the amount of Mn^{4+} ions with a high oxidation state is favorable for catalytic oxidation of ethanol, which leads to the highest TOF for 3D-MnO_2. Therefore, the excellent catalytic property of the 3D-MnO_2 catalyst for ethanol oxidation is primarily due to better low-temperature reducibility, more surface adsorbed oxygen species and Mn^{4+} ions. The reaction mechanism of ethanol oxidation over the MnO_2 catalyst has been discussed in our previous report [37]. First, ethanol can be adsorbed on the Mn^{4+} cation active sites on the surface of 3D-MnO_2 via the donation of a lone pair of electrons from the oxygen atom of the ethanol hydroxyl to form an ethoxide intermediate. Second, the adsorbed ethoxide species undergoes sequential α-C—H bond cleavage to form an adsorbed acetaldehyde under the surface active oxygen. Finally, the adsorbed acetaldehyde is further oxidized to CO_2 and H_2O. The mechanism might be appropriate for the oxidation of ethanol on the 3D-MnO_2 catalyst.

4. Conclusions

1D-MnO_2, 2D-MnO_2 and 3D-MnO_2 with different structures were successfully synthesized using hydrothermal and nanocasting methods. The activity for ethanol oxidation over different MnO_2 catalysts decreased in the following order: 3D-MnO_2 > 2D-MnO_2 > 1D-MnO_2. Mesoporous MnO_2 catalysts, especially 3D-MnO_2, have the best low-temperature catalytic activity for ethanol, which is primarily due to better low-temperature reducibility, more surface adsorbed oxygen species and Mn^{4+} ions. After the addition of 10 vol.% H_2O, the complete oxidation of ethanol to CO_2 was observed at 190 °C on 3D-MnO_2. There was no obvious decrease after the sample was run for 160 h. 3D-MnO_2 exhibits potential for the efficient elimination of ethanol due to its activity and stability.

Appendix A. Supplementary data

Supplementary data associated with this article can be found, in the online version, at http://dx.doi.org/10.1016/j.apcatb.2014.08.044.

References

[1] G. Avgouropoulos, E. Oikonomopoulos, D. Kanistras, T. Ioannides, Appl. Catal. B: Environ. 65 (2006) 62–69.
[2] A. Aranzabal, M. Romero-Sáez, U. Elizundia, J.R. González-Velasco, J.A. González-Marcos, J. Catal. 296 (2012) 165–174.
[3] A.N. Merino, B.P. Barbero, P. Ruiz, L.E. Cadus, J. Catal. 240 (2006) 245–257.
[4] R. Wang, J. Li, Environ. Sci. Technol. 44 (2010) 4282–4287.
[5] G. Litt, C. Almquist, Appl. Catal. B: Environ. 90 (2009) 10–17.
[6] F. Wang, H. Dai, J. Deng, G. Bai, K. Ji, Y. Liu, Environ. Sci. Technol. 46 (2012) 4034–4041.
[7] M.R. Morales, B.P. Barbero, L.E. Cadus, Fuel 87 (2008) 1177–1186.
[8] B. Bialobok, J. Trawczynski, W. Mista, M. Zawadzki, Appl. Catal. B: Environ. 72 (2007) 395–403.
[9] Q. Ye, Q. Gao, X.R. Zhang, B.Q. Xu, Acta Chim. Sin. 64 (2006) 751–755.
[10] M.R. Morales, B.P. Barbero, T. Lopez, A. Moreno, L.E. Cadus, Fuel 88 (2009) 2122–2129.
[11] M.M. Roxana, B.P. Barbero, T. Lopez, A. Moreno, E.L. Cadus, Fuel 88 (2009) 2122–2129.
[12] P.V. Santos, S.A.C. Carabineiro, P.B. Tavares, M.F.R. Pereira, J.J.M. Orfao, J.L. Figueiredo, Appl. Catal. B: Environ. 99 (2010) 198–205.
[13] H. Najjar, H. Batis, Appl. Catal. A: Gen. 383 (2010) 192–201.
[14] H. Li, G. Qi, Tana, X. Zhang, X. Huang, W. Li, W. Shen, Appl. Catal. B: Environ. 103 (2011) 54–61.
[15] N. Hebben, C. Diehm, O. Deutschmann, Appl. Catal. A: Gen. 388 (2010) 225–231.
[16] W. Wang, H. Zhang, G.-d. Lin, Z. Xiong, Appl. Catal. B: Environ. 24 (2000) 219–232.
[17] V. Blasin-Aubé, J. Belkouch, L. Monceaux, Appl. Catal. B: Environ. 43 (2003) 175–186.
[18] P.O. Larsson, A. Andersson, Appl. Catal. B: Environ. 24 (2000) 175–192.
[19] A. Wahlberg, L.J. Pettersson, K. Bruce, M. Andersson, K. Jansson, Appl. Catal. B: Environ. 23 (1999) 271–281.
[20] S.S.T. Bastos, J.J.M. Orfao, M.M.A. Freitas, M.F.R. Pereira, J.L. Figueiredo, Appl. Catal. B: Environ. 93 (2009) 30–37.
[21] D. Delimaris, T. Ioannides, Appl. Catal. B: Environ. 84 (2008) 303–312.
[22] M.R. Morales, B.P. Barbero, L.E. Cadus, Appl. Catal. B: Environ. 67 (2006) 229–236.
[23] B. Bai, H. Arandiyan, J. Li, Appl. Catal. B: Environ. 142–143 (2013) 677–683.
[24] X. Xie, Y. Li, Z.Q. Liu, M. Haruta, W.J. Shen, Nature 458 (2009) 746–749.
[25] L. Hu, Q. Peng, Y. Li, J. Am. Chem. Soc. 130 (2008) 16136–16137.
[26] X. Wang, Y. Li, J. Am. Chem. Soc. 124 (2002) 2880–2881.
[27] J. Zhang, Y. Jin, C. Li, Y. Shen, L. Han, Z. Hu, X. Di, Z. Liu, Appl. Catal. B: Environ. 91 (2009) 11–20.
[28] X. Liang, J. Xiao, B. Chen, Y. Li, Inorg. Chem. 49 (2010) 8188–8190.
[29] B. Lee, D. Lu, J.N. Kondo, K. Domen, J. Am. Chem. Soc. 124 (2002) 11256–11257.
[30] H. Tüysüz, C.W. Lehmann, H. Bongard, B. Tesche, R. Schmidt, F. Schüth, J. Am. Chem. Soc. 130 (2008) 11510–11517.
[31] F. Jiao, A. Harrison, J.C. Jumas, A.V. Chadwick, W. Kockelmann, P.G. Bruce, J. Am. Chem. Soc. 128 (2006) 5468–5474.
[32] J. Luo, Y. Wang, H. Xiong, Y. Xia, Chem. Mater. 19 (2007) 4791–4795.
[33] F. Jiao, J. Jumas, M. Womes, A.V. Chadwick, A. Harrison, P.G. Bruce, J. Am. Chem. Soc. 128 (2006) 12905–12909.
[34] K. Jiao, B. Zhang, B. Yue, Y. Ren, S. Liu, S. Yan, C. Dickinson, W. Zhou, H. He, Chem. Commun. 0 (2005) 5618–5620.
[35] F. Jiao, M.K. Shaju, P.G. Bruce, Angew. Chem. Int. Ed. 44 (2005) 6550–6553.
[36] J. Trawczyński, B. Bielak, W. Miśta, Appl. Catal. B: Environ. 55 (2005) 277–285.
[37] J. Li, R. Wang, J. Hao, J. Phys. Chem. C 114 (2010) 10544–10550.
[38] H. Rotter, M.V. Landau, M. Herskowitz, Environ. Sci. Technol. 39 (2005) 6845–6850.
[39] M.P. Heynderickx, J.W. Thybaut, H. Poelman, D. Poelman, G.B. Marin, J. Catal. 272 (2010) 109–120.
[40] R. Xu, X. Wang, D. Wang, K. Zhou, Y. Li, J. Catal. 237 (2006) 426–430.
[41] Y. Hou, Y. Cheng, T. Hobson, J. Liu, Nano Lett. 10 (2010) 2727–2733.
[42] F. Jiao, P.G. Bruce, Adv. Mater. 19 (2007) 657–660.
[43] C. Nozaki, C.G. Lugmair, A.T. Bell, T.D. Tilley, J. Am. Chem. Soc. 124 (2002) 13194–13203.
[44] A. Rumplecker, F. Kleitz, L.E. Salabas, F. Schuth, Chem. Mater. 19 (2007) 485–496.
[45] C. Wang, L. Sun, Q. Cao, B. Hu, Z. Huang, X. Tang, Appl. Catal. B: Environ. 101 (2011) 598–605.
[46] E.A. Espinal, L. Zhang, C.H. Chen, A. Morey, Y. Nie, L. Espinal, B.O. Wells, R. Joesten, M. Aindow, S.L. Suib, Nat. Mater. 9 (2010) 54–59.
[47] H. Over, P.A. Seitsonen, Science 297 (2002) 2003–2005.
[48] D. Widmann, R.J. Behm, Angew. Chem. Int. Ed. 50 (2011) 10241–10245.
[49] X. Tang, J. Chen, X. Huang, Y. Xu, W. Shen, Appl. Catal. B: Environ. 81 (2008) 115–121.
[50] Y. Shen, Y. Yang, Y. Wang, Y. Zhang, H. Zhu, L. Gao, M. Jia, Appl. Catal. B: Environ. 79 (2008) 142–148.
[51] Y.D. Kim, S.J. Jeong, W.-S. Kim, Chem. Eng. Sci. 64 (2009) 1373–1383.
[52] Y. Wei, J. Liu, Z. Zhao, A. Duan, G. Jiang, C. Xu, J. Gao, H. He, X. Wang, Energ. Environ. Sci. 4 (2011) 2959–2970.
[53] G.G. Xia, Y.G. Yin, W.S. Willis, J.Y. Wang, S.L. Suib, J. Catal. 185 (1999) 91–105.